SINERGI Vol. 23, No. 3, February 2023: 451-466
http://publikasi.mercubuana.ac.id/index.php/sinergi
http://doi.org/10.22441/sinergi.2023.3.016

Optimized Swarm Enabled Deep learning technique for bone tumor detection using Histopathological Image

Dama Anand[1], Osamah Ibrahim Khalaf[2]*, Fahima Hajjej[3], Wing-Keung Wong[4], Shin-Hung Pan[4], Gogineni Rajesh Chandra[5]
[1]Department of Department of Computer Science, Koneru Lakshmaiah Education Foundation, India.
[2]Department of Solar, Al-Nahrain Research Center for Renewable Energy, Al-Nahrain University, Iraq
[3]Department of Information Systems, College of Computer and Information Sciences, Princess Nourah bint Abdulrahman University, Saudi Arabia
[4]Asia University, Taiwan
[5]Department of Department of Computer Science, KKR & KSR Institute of Technology and Sciences, India

Abstract
Cancer subjugates a community that lacks proper care. It remains apparent that research studies enhance novel benchmarks in developing a computer-assisted tool for prognosis in radiology yet an indication of illness detection should be recognized by the pathologist. In bone cancer (BC), Identification of malignancy out of the BC's histopathological image (HI) remains difficult because of the intricate structure of the bone tissue (BTe) specimen. This study proffers a new approach to diagnosing BC by feature extraction alongside classification employing deep learning frameworks. In this, the input is processed and segmented by Tsallis Entropy for noise elimination, image rescaling, and smoothening. The features are excerpted employing Efficient Net-based Convolutional Neural Network (CNN) Feature Extraction. ROI extraction will be employed to enhance the precise detection of atypical portions surrounding the affected area. Next, for classifying the accurate spotting and for grading the BTe as typical and a typical employing augmented XGBoost alongside Whale optimization (WOA). HIs gathering out of prevailing scales patients is acquired alongside texture characteristics of such images remaining employed for training and testing the Neural Network (NN). These classification outcomes exhibit that NN possesses a hit ratio of 99.48 percent while this occurs in BT classification.

Keywords:
Bone cancer;
Deep Learning;
Efficient Net CNN;
ROI Extraction;
XGBoost;

Article History:
Received: August 3, 2023
Revised: September 15, 2023
Accepted: September 19, 2023
Published: October 2, 2023

Corresponding Author:
Osamah Ibrahim Khalaf
Department of Solar, Al-Nahrain Research Center for Renewable Energy, Al-Nahrain University, Iraq
Email:
usama81818@nahrainuniv.edu.iq

INTRODUCTION

Bone cancer (BC) is a group of illnesses defined by uncontrolled cell development. To treat the patient, early discovery and categorization of the bone tumor are required. Here, research proposes a novel technique for detecting BC by feature extraction (FE) with classification using deep learning (DL) architectures. Here, the input has been processed and segmented for noise removal, image resizing, and smoothening [1]. Unusual development of cell which liable to assault. As indicated by the review of individuals with sickness. More than seven lakhs new malignant growth patients enrolled and 556,400deaths on account of disease enlisted each year. Clinically the BC is termed the Sarcomas, which enables within the muscle, bone, fibrous tissue, blood vessels, and few tissues. Few general kinds of BC include osteosarcoma, chondrosarcoma, Ewing's sarcoma, pleomorphic sarcoma, and fibrosarcoma. Concerning BC, the tumor will be created inside the bone and impact the bone's development and motion. Particularly, concerning

the bone tumor (BT) aspect, Enchondroma remains a benign tumors category that is noticed within the bone that starts at the cartilage [2]. Predominantly, Enchondroma will be noticed in the hand's tiny bones – feasible vulnerable bone regions for this include (thigh bone), tibia (shin bone), and humerus (upper arm bone) [3]. BTs' biological conduct differs highly amidst disparate classes [4]. Nevertheless, their medical administration will be chiefly decided by the magnitude of the tumor aggression that will be generally categorized as a benign, intermediary, and malignant [5]. When BT's medical properties and radiological data might assist doctors to arrive at early detection, BT's histopathological analysis (HA) stays definite in defining the BT's biological nature and verifying its aggression. Hence, a precise and dependable histopathological differentiation (HD) remains critical for assuring an adequate sick person result. Dissimilar to tumor or epithelial beginning that remains very common, pathologists' exposure in detecting BTs generally be deficient because of the comparatively less incidence and diverse histological morphology [6]. Furthermore, a few disparate types of BTs might apportion the same histologic morphology due to mesenchymal origin, hence presenting surprising and unusual criteria in classification. Additionally, the diagnostician's prognosis of BT's histopathological classification (HC) that remains inclined to subjectiveness cannot be sufficiently calculated meanwhile [7].

Regarding the disadvantages of conventional HA aforementioned, detection techniques cantered upon artificial intelligence steadily occur alongside the enhanced progression of arithmetical potential and DL [8]. Convolutional Neural Network (CNN) comprises DLs that could be trained for excerpting particular features out of an image database to output a quantifiable probability and construct a classifier. Moreover, the whole slide imaging's (WSI) development facilitates slides digitized as macro data devoid of data losing [9] that remains appropriate for neural networks (NNs) for processing and learning. By employing WSI in recent years, the CNN was validated efficiently in the HC of multiple tumors of epithelial origin (EO) like breast [10], lung, gastric, prostate, and nasopharyngeal cancers [11].

In correlation with EO's tumor, BTs remain chiefly of mesenchymal emergence exhibiting exceptionally disparate and varied microscopic morphology. Nevertheless, it misses pertinent proof concerning the DL-related HC execution for BTs till now. Precise DL-aided differentiation of principal BTs microscopically and qualitatively as a benign, intermediary, and malignant will never merely recompense for the doctor's restricted exposure and prejudiced elucidation, yet as well give a quantitative technique for analysing the BTs' biological nature, which possibly results in a finer medicament option [12]. This research assesses the possibility of employing DL in qualitative HD of primary BTs and correlates the finest paradigm's execution with pathologists of disparate degrees of experience.

When Computer-Aided Diagnosis (CAD) is currently employed in radiology alongside a vast variety of body areas and an array of imaging modalities, the predominant query remains: could CAD facilitate illness diagnosis? Notice that this query, contrasted with many prognostic queries, remains encouraged by the intrinsic restriction in radiological data's spatial resolution. As an example, in mammography, CAD methodologies are established for automatically recognizing or classifying mammographic lesions. In histopathology, contrastingly, just detecting cancer's existence or non-existence, or moreover, cancer's accurate spatial extent might not contain as much attention. This study's apportionments are:

- This work proffers a novel methodology for identifying BC employing DL frameworks for FE and classification. The features are excerpted employing the Efficient Net-based CNN framework for enhancing the precise detection of atypical portions surrounding the affected region (AR).
- To classify the precise spotting and to grade the BTs as typical and atypical employing XGBoost alongside whale optimization algorithm (WOA).

The remaining of this chapter is arranged as: Section 2 highlights some prevailing studies, Section 3 exhibits the proposed technique and methods, Section 4 shows the experiential results and discussion, and, lastly, Section 5 sums up with a conclusion and upcoming research.

PREVIOUS STUDIES

Many advanced pieces of research centred upon DL were identified as the latest chief improvement in HI identification. Nevertheless, a few exertions of image identification remain concentrated upon BC's histopathological images (HIs).

Survey upon deep NN for FE

Sharma et al. [13] puts forth the finest appropriate edge identification algorithm in which 2 feature sets (FSs) – first having hog and second devoid of hog are formulated. For testing the efficacy of such FSs, 2 machine learning (ML) paradigms such as support vector machine (SVM) and Random Forest (RF) will be engaged.

Anisuzzaman et al. [14] embraces transfer learning approaches and pre-trained CNNs for a public database upon osteosarcoma HIs for identifying necrotic images out of non-necrotic and healthful tissues. Initially, the database will be pre-processed, and various classifications will be implemented. Next, transfer learning paradigms incorporating VGG19 and Inception V3 will be employed and trained upon WSIs having nil patches for enhancing the outputs' precision. Lastly, the paradigms will be implemented to disparate classification issues incorporating binary and multi-class classifiers.

Vandana et al. [15] puts forth an optimized Graph Cut-based clustering architecture for determining the malignancy degree in hematoxylin and eosin (H&E) stained HIs. This technique performs repeated Graph Cut methodology (GCM) for excerpting front objects out of biopsy images. Often, GCM requires user communication for initiating the segmentation procedure. Yet, in optimized GCM, the first data will be physically created employing conventional image processing tools. As a result, the experimentation exhibits that the proffered segmentation outcome's quality will be enhanced. Subsequent to the segmentation of entire tissue cells, its classification will be performed via colour and topological attributes. Hence, domain-specific methodologies like colour-related clustering, arithmetical morphology, and active contour will be employed in FE.

Vandana et al. [16] excerpts entire significant features like malignant osteoid, hyperchromatic nuclei, and nuclei number out of the segmented images and divided them into 3 sets. Then, a training set having bottom-order descriptors will be inferred out of every set and employed for training an SVM. Lastly, the technique infers test sets having an unfamiliar class label that is provided for training the SVM classifier.

Nguyen et al. [17] proffers 2 phases-related CNN-related frameworks for automated tumor excerption and tumor kind classification. During the initial step, the tumor will be segmented out of MRI scans employing the proffered 3D CNN framework; following this, the segmented tumor will be classified into 4 classes – T1, T2, T1CE, and Flair – by employing pre-trained VGG-19 CNN. Publicly accessible MRI scans' BraTS databases 2015, 2017, and 2018 will be employed for this function.

Li et al. [18] comprises frameworks having AlexNet and LeNet having three convolutional layers (CLs), 3 sub-sampling layers, and 2 completely joined layers to classify the Osteosarcoma pathology database into a tumor and non-tumor categories. This proffered technique attained 84% accuracy.

Arunachalam et al. [19] Presents a deep CNN (DCNN) paradigm having a Siamese network (DS-NET) crafted for classifying Osteosarcoma images. This proffered model includes an Auxiliary Supervision Network (ASN) and a Classification Network (CN). This study affirms that DS-Net's experiential outcome has a mean precision of 95.1%. VGG-19 and Inception V3 will be employed as pre-trained paradigms upon a publically accessible Osteosarcoma database for binary and multiple class classification.

Survey upon optimal classifier for HIs

Badashah et al. [20] introduces an efficient identification methodology employing the proffered Fractional-Harris Hawks Optimization-based Generative Adversarial Network (F-HHO-based GAN) to identify osteosarcoma in the initial phase. In this, the proffered F-HHO will be crafted by incorporating Fractional Calculus and HHO correspondingly. Consequently, the classification of the feasible tumor, non-tumor, and necrotic tumor will be performed by GAN employing the histology image (HyI) slides.

Lefteh et al. [21] proffers an approach for the BC detection using fuzzy C-mean clustering together with Modified Adaptive Neuro-Fuzzy Inference System (MANFIS) alongside the Artificial Bee Colony algorithm for classifying benign and malignant BC.

Gurav et al. [22] offers the prostate cancer diagnosis methodology employing HIs through proffering the fuzzy-related salp swarm algorithm-based rider NN (SSA-RideNN) classifier. Initially, the input image (II) will be supplied toward the pre-processing phase, and, next, the segmentation will be executed employing Colour Space transition and thresholding. When the segmentation has been executed, the FE will be carried out by excerpting numerous kernel scale-invariant transition features alongside the texture features, which will be excepted centred upon local optimal oriented pattern descriptor for enhancing the classification precision.

Shrivastava et al. [23] crafts an ML methodology for classifying BC. The methodology remained more efficient and attained finer execution. This in no way regards a NN for calculating the dimension, position, and cancer phase.

Santhanalakshmi et al. [24] proffers a BT identification methodology employing Recurrent NN (RNN). The methodology possesses great precision. Nevertheless, this lost to regard

additional pertinent features to enhance classification execution and as well lost to prognosticate intricate images.

Hossain et al. [25] puts forth a methodology employing fuzzy clustering and a neuro-fuzzy classifier to identify BC. This employs an adaptive neuro-fuzzy inference system (ANFIS) in benign and malignant BC's classification. The fuzzy segmentation gives finer execution in bone MR images. Nevertheless, the methodology requires to be updated for intricate BTs.

Prognosticating the initial samples out of the images remains the arduous job to prognosis Osteosarcoma for the prognosis in the initial phase. In this, GAN generates the adversarial game betwixt the generator and discriminator for seeking in any case the sample is acquired out of image or paradigm dispensation to prognosticate the initial samples. Additionally, this methodology employed for osteosarcoma diagnosis must possess great speed optimization networks.

METHODS

This segment addresses the proffered approach in BC identification. At first, pre-processing is performed for lessening the noise within the images by employing a guided and adaptive median filter (AMF). The preprocessing images will be segmented by Tsallis entropy (TE) that executes upon conventional analytical mechanism. The present research proffers a novel methodology to identify BC employing DL frameworks for FE and classification. The features will be excerpted by employing the Efficient Net-based CNN framework for enhancing the precise detection of atypical portions surrounding the AR. Next, for the classification of the precise spotting and grading of the bone tissue (BTe) as typical and atypical, XGBoost alongside WOA is employed as illustrated in the following Figure 1.

Database Description

Osteosarcoma HyI Database was employed in this study. This database could be downloaded out of the Cancer Imaging Archive (TCIA) webpage [25]. This database has been gathered out of 4 sick persons betwixt 1995 and 2015 by a medical researcher crew in the University of Texas South-western Medical Centre at Children's Medical Centre, Dallas. This database can be publicly accessible upon the TCIA webpage for study intentions. This database consists of 1144 Osteosarcoma's H&E stained HyIs containing an image dimension of 1024 × 1024 pels. This database comprises 3 HyIs classes – (a) Non-Tumor (NT), (b) Non-Viable Tumor (NVT), and (c) Viable Tumor (VT). Most of the database class remains NT, which comprises 536 typical tissue images of bone, blood vessels, and cartilage. NVT and VT remain the database's trivial classes having 263 and 345 images accordingly. NVT class comprises images of demise or the recuperation phase tissues possessing a comparatively light colour. VT remains an area within HIs in which nuclei remain closely assembled collectively in dark colour.

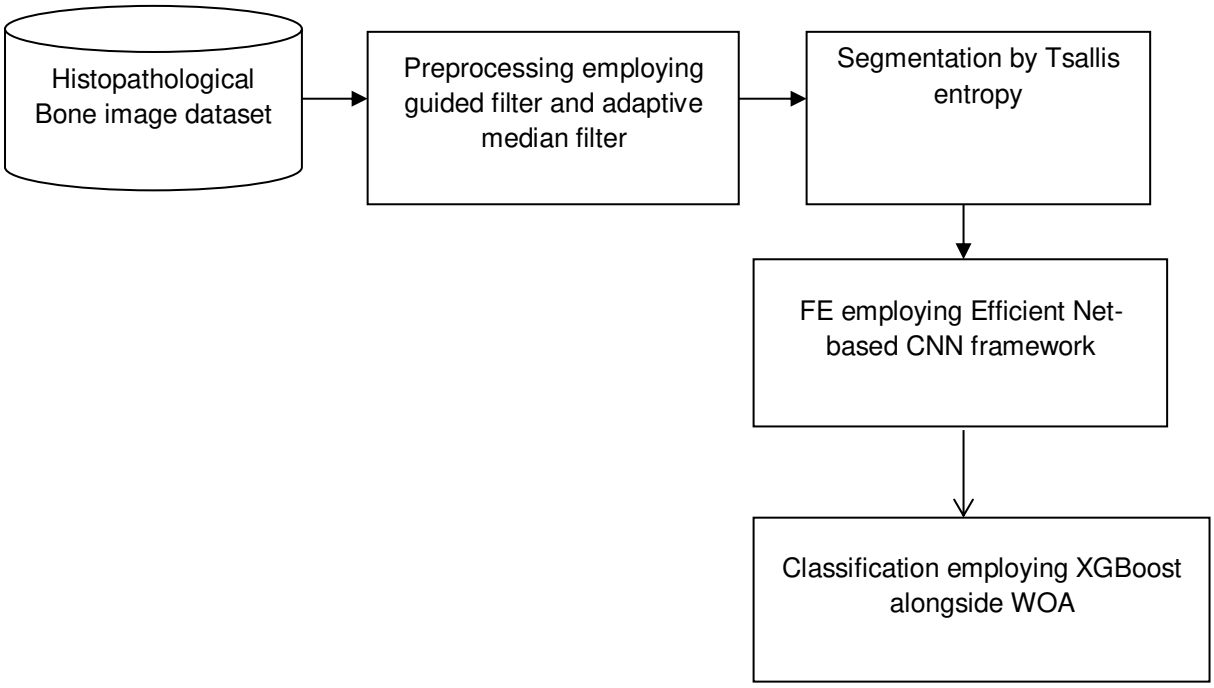

Figure 1. Comprehensive proffered framework for BC classification

Images' Pre-processing

A guided filter (GF) might be regarded as a bilateral filter yet have finer execution close to the edges. Hypothetically, a GF could be joined with the Laplacian matrix. Hence, a GF possesses the extra benefit of employing architecture for creating an enhanced image in comparison with a normal smoothing operant. Additionally, arithmetical intricacy remains independent of the filter's kernel dimension because of the GF's quick and non-approximate linear-time algorithm. A local linear paradigm having I as the guidance image, P as the filtering II, and Q as the filtering output image gives the GF's chief hypotheses. The linear transition will be presumed as Q of P having a window m_k formulated on pel k. The explanations of GF and its kernel are:

$$Q_i = c_k I_i + d_k, \nabla \in w_k \quad (1)$$

In which (c_k, d_k) remains more or less constant linear coefficients in the w_k square window employing radius r alongside the index k. Having II P, lessening the rebuilding error employing Equation (2) amidst P and Q provides the ensuring outcome:

$$c_k = \frac{\sum_{i \in w} \quad I_i p_i - w_k}{\alpha_k - \varepsilon} \quad (2)$$

$$d_k = p_k - c_k w_k \quad (3)$$

In which w_k and α_k represent the mean and variance of *I* in the window, and ε represents the regularization criterion managing the smoothness level. Subsequent to computing (c_k, d_k) for entire patches w_k within the image, the filter output will be computed by:

$$Q_i = c_i I_i + d_i \quad (4)$$

In which c_i and d_i represent the entire windows' mean coefficients formulated on *i*. Owing to the reinforcement of AMF, the filtration could be enhanced as ensues. Consider $\left\{\left\{y_{i,j}^{(0)}\right\}, \{y_{i,j}^{(1)}\}, \ldots . \{y_{i,j}^{(0)}\}\right\}$ as grayscale images' concatenation and $\left\{\left\{g_{i,j}^{(0)}\right\}, \{g_{i,j}^{(1)}\}, \ldots . \{g_{i,j}^{(0)}\}\right\}$ as a concatenation of contorted pels's maps where the values $g_{i,j}^{(n)}$ are defined relying upon the existence of contortion in the pel $y_{i,j}^{(n)}$ by,

$$g_{i,j}^{(n)} = \{0, if\, y_{i,j}^{(n)} isnotdistorted\ 1, if\, y_{i,j}^{(n)} isdistort \quad (5)$$

The notation $y_{i,j}^{(0)}$ is employed for the initial noisy image. $y_{i,j}^{(n)}$ Represents the pel value having coordinates (i, j) subsequent to the methodology's n-th repetition. In the maps' concatenation of contorted pels $g_{i,j}^{(n)}$ and $g_{i,j}^{(n)} = 0$ refers to a pel having coordinates (i, j) that remains undistorted and the value 1 $g_{i,j}^{(n)}$ refers to a pel having coordinates (i, j) that remain undistorted and requires to be set.

Tsallis entropy-related segmentation

As the images are compiled of pixels containing discrete gray levels, this discourse would be performed via a discrete set of probabilities $\{p_i\}$ having random variable$i$. Subject to probabilities remain $\Sigma i p_i = 1$.

For whatsoever actual *q*, TE can be explained by,

$$s_q = \frac{k}{q-1}[1 - \sum \quad p_i^q] \quad (6)$$

Where q represents the 'entropic index', and k represents a constant in which the image processing is fixed to one. Contemplate 2 individual classes A and B possessing joint probability - $p(A, B) = p(A)\, p(B)$. The entropy $S(AUB)$ remains $S(A) + S(B)$. the classes could be provided as in the ensuing. Class A comprises images having gray tones labeled $\{x_1, x_2 \ldots x_t\}$; for example, $\{0,1,2, \ldots, t\}$ have gray tones less than the provided threshold t. Presume that every tone x_i will be selected $N_{A,t}$ times as per the frequency. The bi-level threshold t for the gray levels having the TEs is:

$$s_q(t) = s_q^A(t) + s_q^B(t) + (1 - q) s_q^A(t) s_q^B(t) \quad (7)$$

FE employing EffecientNet-based CNN framework

The EfficientNet family remains centred upon a novel methodology for enhancing CNN paradigms. This employs an uncomplicated and very efficient compound coefficient. Disparate out of the conventional methodologies, which scale networks' sizes like breadth, deep, and resolution, EfficientNet scales every size with a fastened array of scaling coefficients consistently. Essentially, scaling independent sizes enhances the paradigm's exertion; nevertheless, standardizing the entire network's sizes concerning the accessible resources efficiently enhances the comprehensive execution. The neurons within the initial CL catch the features within a tiny region inside the image. When the filters' dimension employed remains 3 × 3, it would remain this region's dimension. The region is referred to as the receptive field (RF) of the particular neuron within the image. As we move

deeper and deeper inside the network, every neuron correlates to a bigger and bigger RF. Global Average Pooling (GAP) executes an uncomplicated mean having equivalent weights that in no way provide whatsoever distinctive attention to specific RFs or II's areas. The proffered paradigm for FE is called EfficientNet-CNN and is illustrated in Figure 2.

Hence, the GAP procedure executes the procedure as exhibited in the following equation:

$$L_j = GAP(L_{j-1}) = \frac{1}{M \times M} \sum_{i=0}^{M \times M} F_i \qquad (8)$$

in which L_j and L_{j-1} represent the GAP function's input layer (IL) and output layer (OL), F_i represents the feature vectors (FVs) present in the layer L_j, and MxM represents the FVs' count. For applying attention, a weighted mean should be calculated by:

$$L_j = GAP\_ATN(L_{j-1}) = \sum_{i=0}^{M \times M} w_i F_i \qquad (9)$$

in which w_i and F_i represent the weights to be learnt by the paradigm automatically. The network layer's committed branch is included in the paradigm for learning the very appropriate weights out of every image, which concentrates attention upon its pertinent area. It could be implemented to whatsoever feature map (FM) within the CNN paradigm. Presume the input FM's dimension as N × N × C in which N × N denotes the two-dimensional map dimension and C denotes the channels' quantity. The attention module begins by squeezing the FM by employing 2 successive CLs thereby the dimension remains N×N×16. Next, this employs a locally joined two-dimensional layer ensued by a sigmoid activation function (AF) for learning N×N weights. Next, one more CL will be employed for replicating the weights through the channel size C times. This remains significant for noticing that this layer will be ensued by a linear AF that refers that the weights could embrace a vast extent of values.

Generally, deep paradigms will be trained end-to-end employing the back propagation approach lessening the cross-entropy loss.

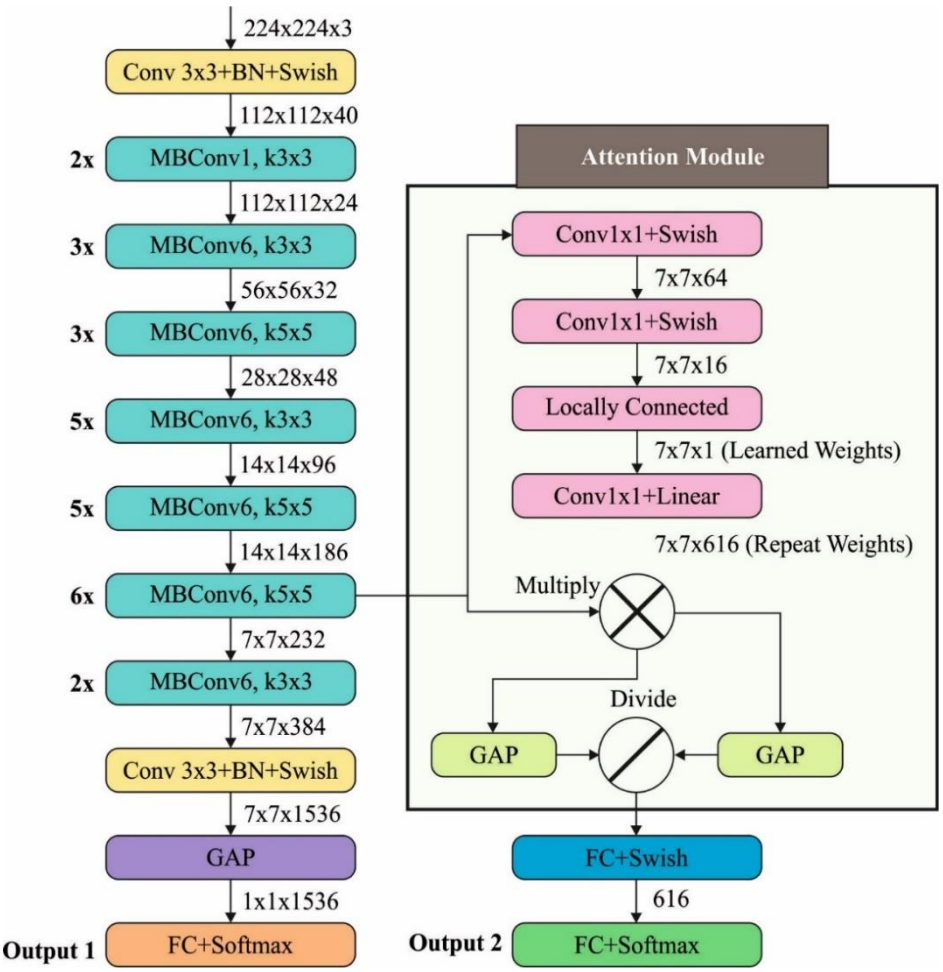

Figure 2. EfficientNet-CNN-based FE framework

$$E = -\frac{1}{n}\sum_{I=1}^{N} \sum_{K=1}^{C} 1(Y_{ik} = k) ln(\frac{expexp\,(w_k^{out})\, h_k^{out}}{\sum_{j=1}^{c} exp(w_k^{out}) h_k^{out}}) \quad (10)$$

In which n represents the training samples' quantity, C represents the class quantity, Y_{ik} represents the prognosis probability for sample i and class k, h_k^{out} represents the final hidden layer's output and w_k^{out} represents the weight matrix from this hidden layer toward the OL. Formulation 1(·) represents an indicator function, which considers one when the statement remains real or this considers zero.

Down sampling Scale lessening an attention mechanism

For choosing the finest-executed down sampling scale (DS), numerous and detailed experimentations have been performed upon the DS [2,4,6,8,16], and Strategy 16 surpasses the rest of the settings. The FM's dimension in the finest-executing DS (16) remained 6 × 6 that be a single time bigger than the initial down sampling multiple (32). For an instance for the attention mechanism (AM), this could be observed in Figure 3 that the reply to the background remains big as many portions of the image comprise the background. Nevertheless, this data generally remains unrequired for classification, and, hence, the reply must be oppressed. Contrastingly, cancerous tissue remains very informational and claims greater activation; thus, its reply will be optimized subsequent to being processed by the AM.

The AM applied by a Squeeze-and-Excitation (S&E) block is embraced in this study, which was proffered by Hu et al. [61]. Succinctly, the requisite elements remain the S&E. If FMs U possess C channels, the feature dimension within every channel remains$H * W$. For the Squeeze operation (SO), GAP can be implemented to U facilitating features for obtaining a global receptive field. Subsequent to the SO, the FM's dimension U modifies from $H * W * C$ to $1 * 1 * C$. Outcomes will be portrayed as Z. Very accurately, this modification is provided as,

$$z_c = F_{sq}(u_c) = \frac{1}{H \times W}\sum_{i=1}^{H}\sum_{j=1}^{H} U_c(i,j) \quad (11)$$

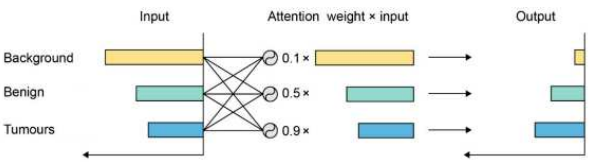

Figure 3. Attention Layer portrayal in Efficient Net-CNN

In which c represents U's c^{th} channel, and F_{sq} represents the Squeeze function. Subsequent to the SO, the Excitation operation (EO) remains for learning disparate channels' weight (scalar) that remains plainly applied by the gating mechanism. Particularly, 2 completely joined layers will be ordered for learning the features' weight and activation function sigmoid, and Rectified Linear Unit (RELU) will be implemented for non-linearity (NL) enhancement. Excluding the NL, the sigmoid function as well confirms the weight falls to the extent of $[0,1]$. the scalar's (weight) computation procedure is exhibited in (12)

$$S = F_{ex}(Z,W) = \sigma\big(g,(Z,W)\big) = \sigma(W_2\delta(W_1 Z)) \quad (12)$$

in which S represents the EO's outcome, F_{ex} represents the Excitation function, g represents the gating function, σ and δ represent the sigmoid and RELU function accordingly, and W_1 and W_2 represent the learnable criteria of the 2 completely joined layers. The last result will be computed by multiplying the scalar S with the initial FMs U.

Feature fusion layer

The 4 phases incorporated in the feature fusion (FF) approach are exhibited in Figure 4. (a) In the forward procedure, the CLs' output (features) is stored in the fourth, seventh, seventeenth, and twenty-fifth blocks. (b) Subsequent to the final CL excerpted features, the AM will be implemented to features registered in phase one for valuing the important data. (c) Bottom-order and upper-order features will be amalgamated by employing Phase 2's outputs subsequent to implementing the AM. (d) Such fused features will be later forwarded towards the ensuing layers for performing classification.

Classification employing XGBoost alongside whale optimization algorithm

Subsequent to the optimal choice of the bone database's feature, an optimal XGBoost will be employed for images' optimal classification.

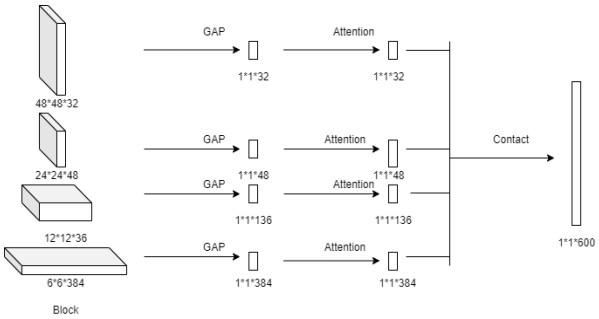

Figure 4. FF procedure with sequence

In this study, WOA is as well employed to craft an optimal classifier-related NN. The chief notion in this research remains in optimizing the weights' value for attaining a global optimal NN-related classifier.

XGBoost's central conception remains in learning novel features by including a tree framework, equipping the residuals of the last prognosis, and, later, acquiring the sample score. By including every tree's scores, the sample's last prognosis score could be acquired. For *n* samples having *m* features, the equation for prognosticating scores having K addition functions remains:

$$y' = \sum_{k=1}^{k} \quad f_k(x_i), f_k \in F \qquad (13)$$

In which F represents the regression tree's (RT) space, $f(x)$ remains an RT that portrays the individual framework score of every –leaf tree. XGBoost transitions the intended action's optimization issue into the issue of seeking the quadratic function's minimal value and employs the loss function's second inferential data for training the tree paradigm. Simultaneously, the tree intricacy will be included as a usual term for the intended action for preventing the over fitting issue. XGBoost's intended action remains:

$$\text{L (H) =-}\alpha\sum_{i}^{n} \quad log\ log\ (pi)\ - \sum_{i}^{n-1} \quad (1 - pi) \qquad (14)$$

Ensuing boosting weights' standard conventional deriving, the sample j's weight within the positive bag is:

$$w_{ij} = \frac{1-pi}{pi} \text{ .pij} \qquad (15)$$

The weight for samples within the negative bags is:

$$w_{ij}{}^{\text{‘}} = \text{pij} \qquad (16)$$

Every boosting round remains for seeking the frail classifier h(x) which lessens. The consequential robust classifier remains H(x) = P_{λ}tht(x). λ_t is found employing line search for lessening L (H + $\lambda_t h_t$). WOA assists in optimizing the training process's speed by employing optimally choosing the criteria pel resolution. WO approach's functioning standard remains that the humpback whales poach the prey employing operand– searching the prey, encompassing the prey, and creating a bubble net for the poaching procedure. WOA's comprehensive procedure will be undoubtedly mentioned herein. The mathematical portrayal of encompassing the prey, spiral bubble-net feeding acts, and finding prey will be exhibited in this segment.

Step 1: Initialization

This step of the proffered algorithm can be created by establishing the original resolution haphazardly. As an example, subsequent to BC's HI pre-processing, its pel dimension is created by the CNN's criteria that can be ideally chosen with the aid of the proffered optimization algorithm. In this, the CNN's criteria such as kernels count, padding, pooling kind, FMs count, and whales count (known as whale populace) will be haphazardly initialized. Hence, haphazard value in the search space can be portrayed by:

$$E(u) = (e1, e2, \ldots eh) \qquad (17)$$

In this, E indicates the whale's initial populace at h, which portrays the interlinked layers' count for optimization.

Step 2: Fitness computation

For automated BC identification, the fitness function (FF) will be created for attaining the finest classification evaluation by optimizing its accuracy and is measured centred upon the following equation:

$$fitness_{fun} = (i)\ \_accuracy \qquad (18)$$

Step 3: Update the location of the present resolution - Encompassing the prey

In this step, the whales' poaching procedure begins when observing the prey's location, and, next, they would encompass the prey. Later, the finest resolution (whale) can be detected that is regarded as the best whale. Towards this finest whale, the rest of the whales would advance subsequent to updating its location. Whales' updated process can be exhibited as the ensuing expressions:

$$v \rightarrow = H \rightarrow E \rightarrow best(u) - E \rightarrow (u) \qquad (19)$$

$$E \rightarrow (u+1) = E \rightarrow best(u) - C \rightarrow V \rightarrow \qquad (20)$$

In which *u* portrays the present repetition, *E*→ finely describes the finest resolution that portrays the present location, *C*→ and *H*→ portray coefficient vectors (CVs), and |C *H| portrays the absolute point. Furthermore, the CVs are arithmetically portrayed as C→=2c→·0→-c→ and H→=2·0→ in which c→ represents a concatenation of iterations linearly from 2 to 0, →∈ (0, 1) for the two exploration and exploitation stages.

Exploitation stage:

This stage can be as well mentioned as the bubble-net attacking approach. It has 2 procedures:

a. Shrinking encompassing procedure: This is arithmetically provided by the ensuing expression:

$C \rightarrow = 2c \rightarrow \cdot o \rightarrow -c \rightarrow$ in which $c \rightarrow$ value will be lessened for arriving at this execution. In this, $c \rightarrow$ will be employed for the lessening of disparage extents of $c \rightarrow$. Else, this is mentioned that the interim extends out of $[-c, c]$, $C \rightarrow$ represents an accidental point in which c can be lessened from two to zero. The seeking representative's novel position could remain disparate whenever $C \rightarrow \in [-1,1]$.

b. Spiral updating location: This can be computed betwixt the prey and the whale's location that can be inferred by:

$$E \rightarrow (u+1) = V \rightarrow Dist \cdot expmts \cdot cos(2\prod s) + E \rightarrow best(\quad (21)$$

In which $VDist = |E \rightarrow best(u) - E \rightarrow (u)|$. this predetermines the distance among the y-th whale and the prey that is indicated as the finest resolution attained till now and is presumed to consider value out of$[-1,1]$. m Portrays the logarithmic spiral's figure. When executing optimization, the whale's position possesses a probability of 50% by choosing whatsoever of the shrinking or spiral encompassing paradigm. Its arithmetical expression remains:

$$E \rightarrow (u+1) = \{E \rightarrow best(u) - C \rightarrow \cdot V \rightarrow, if P < 0.5 VDist \rightarrow$$

$$\cdot expmts \cdot cos(2\prod s) + E \rightarrow best(u), if P \geq 0.5 \quad (22)$$

In which $P \in [0,1]$. Hence, the humpback whales haphazardly seek their prey to create a bubble net.

Exploration stage:

This stage is as well called searching the prey. The following expressions explain the arithmetical format of this stage.

$$V \rightarrow = |H \rightarrow \cdot E \rightarrow random - E \rightarrow | \quad (23)$$

$$E \rightarrow (u+1) = |E \rightarrow random - C \rightarrow \cdot V \rightarrow | \quad (24)$$

The present populace's haphazard location can be portrayed as $E \rightarrow random$. While doing the updating procedure of every resolution, the fitness computation can be measured for seeking the best resolution amidst these. Centered upon the acquired finest resolution, an array of new resolutions is identified, and the FF can be computed for carrying on the top resolution updating procedure.

Step 4: Termination parameter

Lastly, this contends the XGBoost's best criteria by the whale's poaching conduct. Consequently, for seeking the optimal solution or finest FF, the prognosis paradigm will be authorized. As the intended action remains in enhancing the training data's accuracy, the prognosis paradigm acquired for the finest fitness framework can be nicely authorized for prognosticating the unfamiliar data.

Whale Optimization Algorithm (WOA)

Start the whale populace $x_i(i = 1,2,\ldots n)$
Compute fitness function value
Haphazardly choose the search agent X'
When t=1 and t< maximal reiterations
For every search agent
Update a, A, C, l and p
When 1 (p<0.5)
When 2(A<1)
Update the location of the present search agent as per the expression (19)
Otherwise when 2 (A≥1)
Update the location of the present search agent as per the expression (20)
End when 2
Otherwise when 1 (p≥ 0.5)
Update the location of the present search agent by the expression (21)
End when 1
End for
Examine whether whatsoever search agent surpasses search space otherwise change it
Compute the fitness function value
Update x' when this remains finer
T=t+1
End while
Return x'

Testing stage

Subsequent to the completion of the training procedure, the proffered paradigm has been tested with a few arrays of images in the testing stage. For these images, precision, recall, F1-measure, and accuracy for every class were calculated. By computing these metrics, comprehensive accuracy will be produced. The very captivating portion of the proffered algorithm remains that the proffered Efficient Net_CNN framework excerpts an image's features locally –

this refers to the network that would learn particular formats inside the image and could be capable of identifying this anyplace within the image. The phases would be reiterated till the image remains scanned. For acquiring an effectual feature classification, the input data's quantity must be exact – that is, the tiny data's employment leads to enormous mistakes having less accuracy, and contrastingly, the additional data's employment creates data over fitting. These two create the system accuracy for acquiring false rates' great percentage.

RESULTS AND DISCUSSION

This methodology remains constructed upon the Efficient Net_CNN paradigm and applied centred upon the PyTorch DL architecture employing Python. GTX 2080Ti GPUs' 4 portions have been utilized for speeding up the training. Entire paradigms have been trained for thirty epochs. The gradient optimizer remained Adam. Prior to supplying to the network, images have been normalized as per the mean and standard deviation upon their RGB channels. Furthermore, to the RCC, haphazard horizontal and vertical flipping have also been utilized in the training duration for enhancing the databases. While doing the training, the original learning rate remained at 0.003 which has been decayed by a ten factor at the fifteenth and twenty-third epochs. The batch dimension remained 256. The criteria of the enriched EfficientNet and the rest of the corresponding paradigms have been positioned as near as feasible for optimizing the reliability of the correlation experimentation.

Table 1. Processing of bone tumor image using the proposed technique

Class	Source	Pre-processed	Segmented	Output
Necrotic	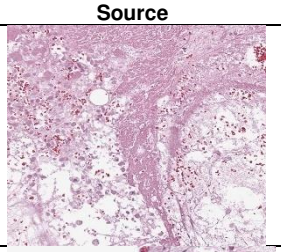	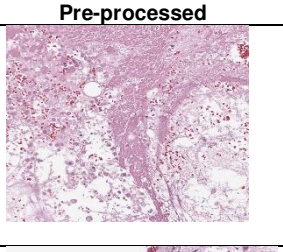	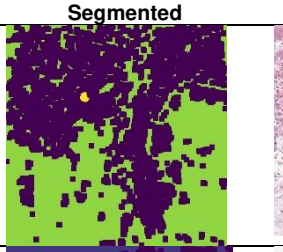	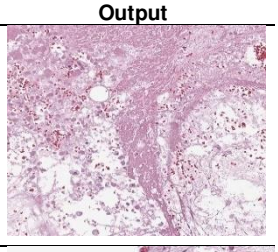
	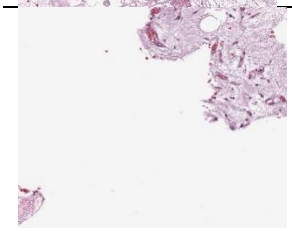	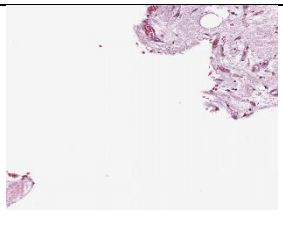		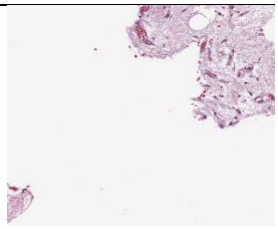
	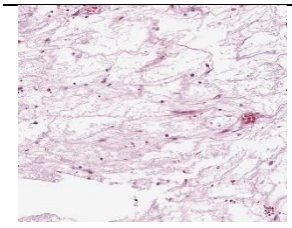	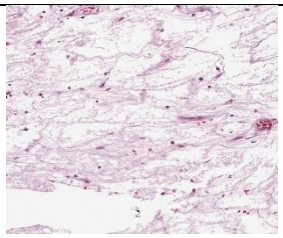	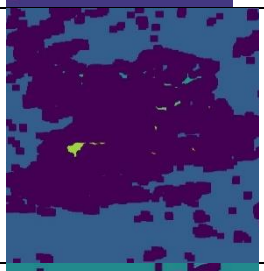	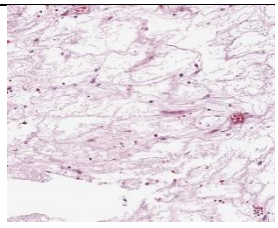
Non-Tumor	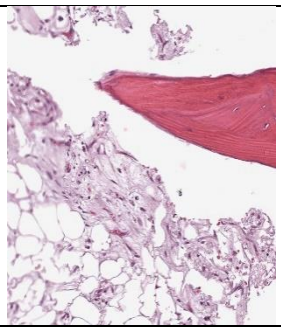	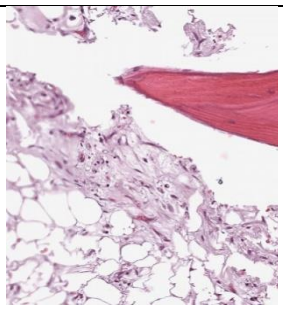		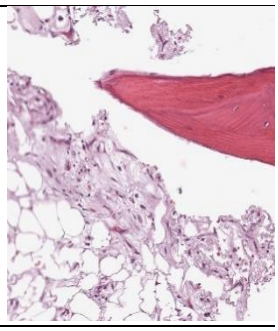

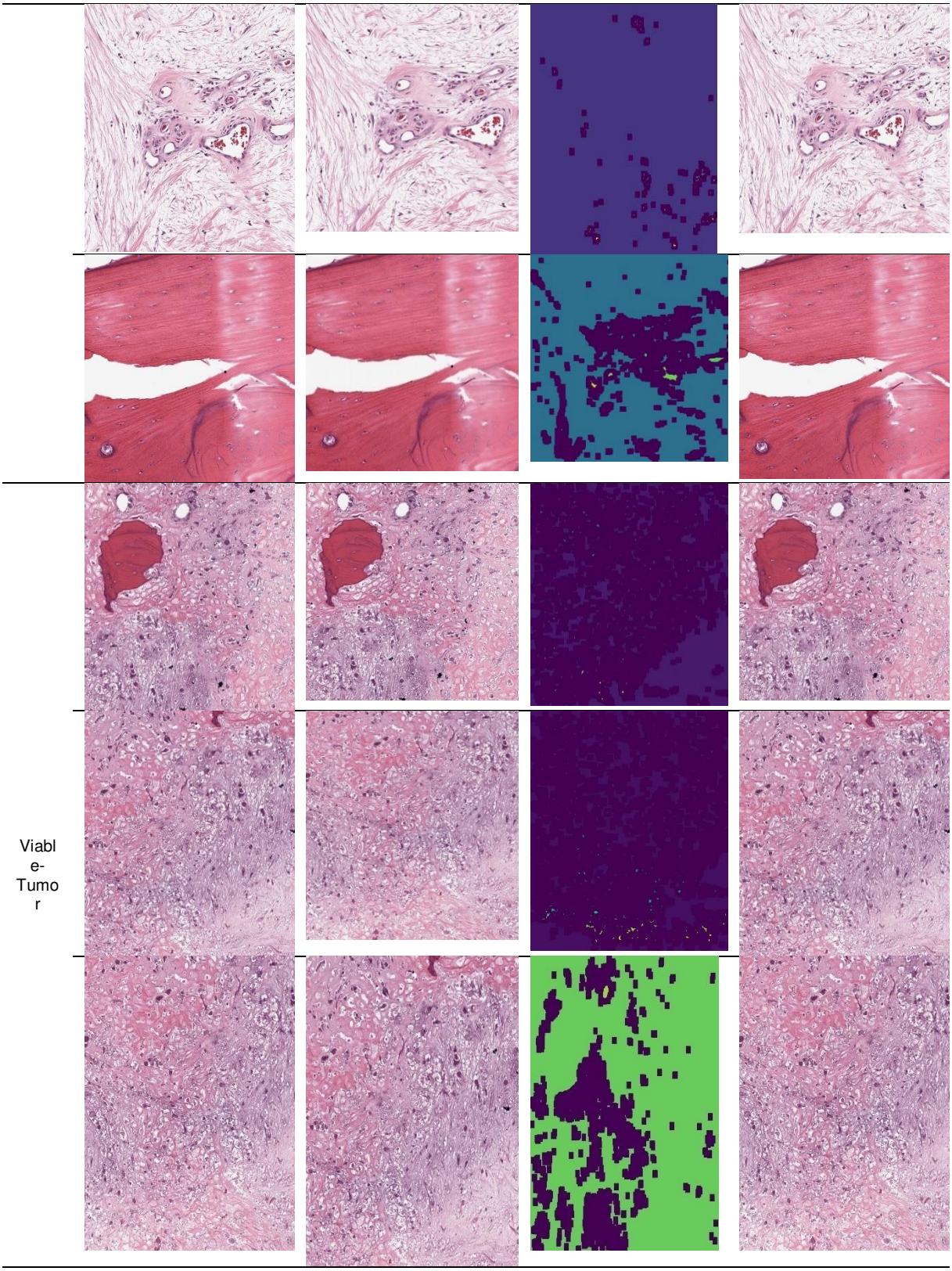

Results and Discussion for Different performance Metric Measures

The disarray matric considered assessment depends on the assessment of different boundaries like exactness, accuracy, review, and F1 - Score. The expressed boundaries are assessed with the assessment of True Positive

(TP), False Negative (FN), True Negative (TN), and False Positive (FP).

Accuracy: This is depicted as the total precisely anticipated values to the total quantity of prognosis as in equation (18)

Accuracy=(TP+TN)/(TP+TN+FP+FN) (18)

Recall: It is the precisely predicted values to the total prediction values as in (19)

Recall=TP/(TP+FN) (19)

Precision: It is the TP values to the total anticipated values as in equation (20)

Precision=TP/(TP+FP) (20)

F1 - Score: This remains the proportion of average precision and recall as mentioned in (21)

F1-Score=2*(Precision*Recall)/(Precision+Recall)

Confusion matrix for cancer diagnosis employing the proffered methodology:

The convolutional layer comprises a few element maps. Every neuron of a similar element map is utilized to remove neighbourhood attributes of various situations in the previous. Notwithstanding, to get another component, the information right off the bat convolved with the initiation work.

The Figure 5 shows the confusion matrix for proposed bone cancer detection techniques based on deep learning. Here the confusion matrix has been taken for the predicted class and actual class of bone cancer detection.

Correlation of the proffered Efficient Net_CNN has been performed with the prevailing methodologies like DCNN, Fractional-Harris Hawks Optimization-based Generative Adversarial Network (F-HHO_GAN).

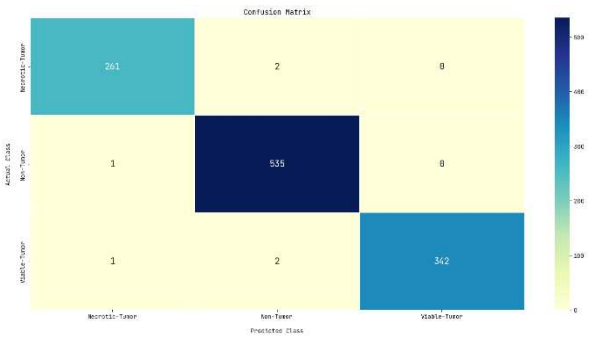

Figure 5. Confusion matrix

Table 1. Accuracy correlation

No. of epochs	DCNN	F-HHO_GAN	Efficient Net_CNN
100	70	75	89
200	75	77.6	84.2
300	78.2	82	86.3
400	81.2	84.7	87.5
500	83.4	85	89.2

Figure 6 illustrates the accuracy in the prevailing DCNN and F-HHO_GAN with the proffered EfficientNet_CNN methodology. The X-axis and the Y-axis exhibit the epochs' quantity and the accuracy values acquired in percentage accordingly. While correlating, the prevailing methodology attains 78.2% and 81.2%, whereas the proffered methodology attains 7.6% finer than DCNN and 4% finer than F-HHO_GAN.

Figure 7 illustrates the precision in the prevailing DCNN and F-HHO_GAN with the proffered EfficientNet_CNN methodology. The X-axis and the Y-axis exhibit the epochs' quantity and the precision values acquired in percentage accordingly.

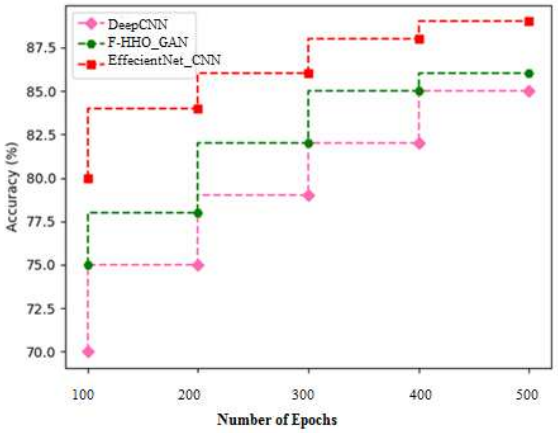

Figure 6. Accuracy correlation

Table 2. Precision comparison

No. of epochs	DCNN	F-HHO_GAN	EfficientNet_CNN
100	71	73	78.1
200	76.2	76.2	81.2
300	80	81.3	84.3
400	81.2	83.4	86.5
500	85.4	84.3	90

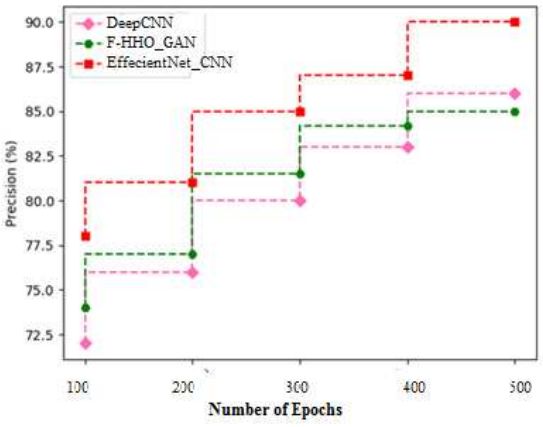

Figure 7. Precision correlation

While correlating, the prevailing methodology attains 79.4% and 80.34% whereas the proffered methodology attains 5% finer than DCNN and 4% finer than F-HHO_GAN.

Figure 8 illustrates the recall in the prevailing DCNN and F-HHO_GAN with the proffered EfficientNet_CNN methodology. The X-axis and the Y-axis exhibit the epochs' quantity and the recall values acquired in percentage accordingly. While correlating, the prevailing methodology attains 69.4% and 71.54% whereas the proffered methodology attains 5.6% finer than DCNN and 3.2% finer than F-HHO_GAN.

Figure 9 illustrates the F1-Measure in the prevailing DCNN and F-HHO_GAN with the proffered EfficientNet_CNN methodology. The X-axis and the Y-axis exhibit the epochs' quantity and the F1-Measure values acquired in percentage accordingly. While correlating, the prevailing methodology attains 66% and 68.6% whereas the proffered methodology attains 5.4% finer than DCNN and 3.2% finer than F-HHO_GAN.

Table 3. Recall correlation

No. of epochs	DCNN	F-HHO_GAN	EfficientNet_CNN
100	61	63	68.1
200	66.2	66.2	71.2
300	71.2	72.5	75.3
400	72.5	75	77.2
500	76.4	79.4	80.1

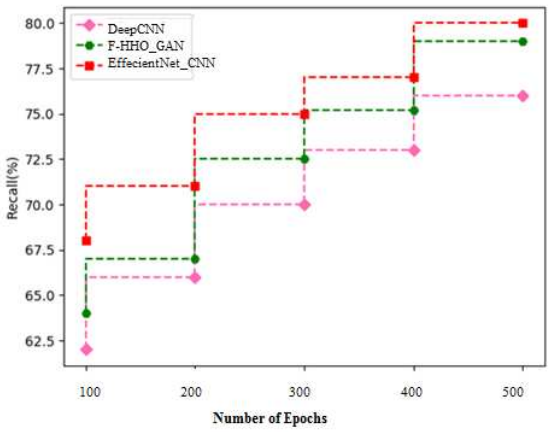

Figure 8. Recall correlation

Table 4. F1-Measure correlation

No. of epochs	DCNN	F-HHO_GAN	EfficientNet_CNN
100	60.1	61.4	65.3
200	61.2	65	67.9
300	66.5	69.3	71.3
400	70.5	71.3	73.2
500	71.4	74.4	77.5

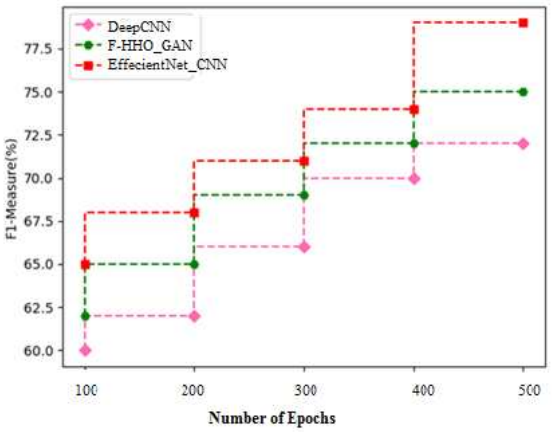

Figure 9. F1-Measure correlation

Table 5 gives the Overall Comparative analysis of the Existing and proposed techniques and in where the proposed techniques EfficientNet_CNN infer the highest performance metrics.

For substantiating that the proffered EfficientNet_CNN remains finer than the prevailing methodologies like DCNN with a Siamese network (DS-Net), the graphs are provided herein. Table 6 exhibits the comprehensive parametric correlation centred upon tumor classes.

Figure 10 exhibits the comprehensive parametric correlation concerning the accuracy, sensitivity, and specificity. The accuracy attained by the proffered EfficientNet_CNN approach remains 99.48%, sensitivity attained remains 99.39%, and specificity attained remains 99.71%. The prevailing DS-Net attains 98% of accuracy, 98% of sensitivity, and 98% of specificity. Figure 11 illustrates the ROC curve.

Table 5. Overall comparative analysis

Parameters	Deep CNN [19]	F-HHO_GAN [20]	EfficientNet_CNN (proposed)
Accuracy	84.1	85	89.2
Precision	85	84	90
Recall	76	79	80
F1-score	71	74.6	77.6

Table 6. Comprehensive parametric correlation centred upon tumor classes

Tumor class	Accuracy	Sensitivity	Specificity
Necrotic-Tumor	0.9965	0.9924	0.9977
Non-Tumor	0.9956	0.9981	0.9934
Viable-Tumor	0.9974	0.9913	1.0

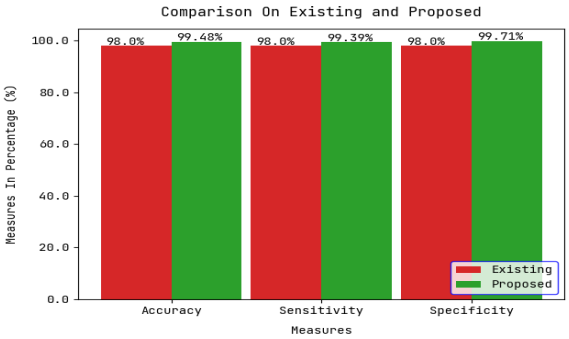

Figure 10. Comprehensive parametric correlation

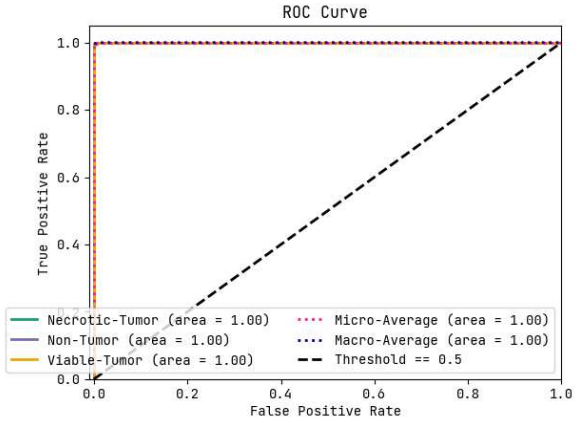

Figure 11. ROC curve for the proffered approach

CONCLUSION

The proffered paradigm executes the identification procedure by incorporating stages such as pre-processing, cell segmentation (CS), FE, and tumor identification. At first, the input H&E stained HyI would be forwarded towards pre-processing unit in which the noise and the outward artifacts would be eliminated out of the II. Nevertheless, the pre-processed image would be supplied towards the CS phase in which the CS procedure would be performed employing the TE-based hybrid fusion paradigm. The features were excerpted employing EfficientNet-based CNN FE, and ROI excerption could be employed for enhancing the accurate detection of atypical portions surrounding the AR. Next, for classifying the precise spotting and for grading the BTe as typical and atypical optimized XGBoost alongside WO has been employed. Out of the assessment, it could be indicated that the proffered technique attained finer execution employing the metrics such as accuracy, sensitivity, and specificity as 99.48%, 99.5%, and 99%. The upcoming facet of this study would implement the DL classifier to identify osteosarcoma – i.e., the upcoming study could amalgamate a DL-related semantic features classification system alongside a Bayesian network technique for optimizing precision.

REFERENCE

[1] T. Altameem, "Fuzzy rank correlation-based segmentation method and deep neural network for bone cancer identification," *Neural Computing and Applications*, vol. 32, no. 3, pp. 805-815, 2020, doi: 10.1007/s00521-018-04005-8

[2] B. S. Vandana, P. J. Antony, and R. A. Sathyavathi, "Analysis of malignancy using enhanced graph cut-based clustering for diagnosis of bone cancer," *Information and Communication Technology for Sustainable Development*, pp. 453-462, 2020, doi: 10.1007/978-981-13-7166-0_45.

[3] D. Shrivastava, S. Sanyal, A. K. Maji, and D. Kandar, "Bone cancer detection using machine learning techniques," *Smart Healthcare for Disease Diagnosis and Prevention*, vol. 20, pp. 175-183, 2020, doi: 10.1016/B978-0-12-817913-0.00017-1.

[4] W. Li, G. G. Wang, and A. H. Gandomi, "A survey of learning based intelligent optimization algorithms," *Archives of Computational Methods in Engineering*, vol. 28, no. 5, pp. 3781– 3799, 2021, doi: 10.1007/s11831-021-09562-1.

[5] G. G. Wang, A. H. Gandomi, A. H. Alavi, and D. Gong, "A comprehensive review of krill herd algorithm: variants, hybrids and applications," *Artificial Intelligence Review*, vol. 51, no. 1, pp. 119-148, 2019, doi: 10.1007/s10462-017-9559-1.

[6] P. Agarwal, A. Yadav, P. Mathur, V. Pal & A. Chakrabarty, "BID-Net: An Automated System for Bone Invasion Detection Occurring at Stage T4 in Oral Squamous Carcinoma Using Deep Learning", *Computational Intelligence and Neuroscience*, vol. 2022, ID: 4357088, 2022, doi: 10.1155/2022/4357088.

[7] J. Y. Kim, D. Kim, K. J. Jeon, H. Kim & J. K. Huh, "Using deep learning to predict temporomandibular joint disc perforation based on magnetic resonance imaging," *Scientific Reports*, vol. 11, no. 1, pp 1-9, 2021, doi: 10.1038/s41598-021-86115-3.

[8] X. Zhang, H. Li, C. Wang, W. Cheng, Y. Zhu, D. Li, & D. Pang, "Evaluating the accuracy of breast cancer and molecular subtype diagnosis by ultrasound image deep learning model," *Frontiers in oncology*, vol. 11, pp. 606, 2021, doi: 10.3389/fonc.2021.623506.

[9] B. Pandey, D. K. Pandey, B. P. Mishra & W. Rahman, "A comprehensive survey of deep learning in the field of medical imaging and medical natural language processing: Challenges and research directions" *Journal of King Saud University-Computer and*

Information Sciences, vol. 34, no. 8, Part A, pp. 5083-5099, 2021, doi: 10.1016/j.jksuci. 2021.01.007

[10] Q. Zheng, L. Yang, B. Zeng, J. Li, K. Guo, Y. Liang & G. Liao, "Artificial intelligence performance in detecting tumor metastasis from medical radiology imaging: A systematic review and meta-analysis" *EClinicalMedicine*, vol. 31, ID: 100669, 2021, doi: 10.1016/j.eclinm.2020.100669

[11] L. R. Yeh et al., "A deep learning-based method for the diagnosis of vertebral fractures on spine MRI: retrospective training and validation of ResNet", *European Spine Journal*, vol. 31, no. 8, pp. 2022–2030, 2022, doi: 10.1007/s00586-022-07121-1

[12] D. M. Anisuzzaman, H. Barzekar, L. Tong, J. Luo & Z. Yu, "A deep learning study on osteosarcoma detection from histological images", *Biomedical Signal Processing and Control*, vol. 69, ID: 102931, 2021 doi: 10.1016/j.bspc.2021.102931.

[13] A. Sharma, D. P. Yadav, H. Garg, M. Kumar, B. Sharma & D. Koundal, "Bone Cancer Detection Using Feature Extraction Based Machine Learning Model" *Computational and Mathematical Methods in Medicine*, vol. 2021, Article ID 7433186, pp. 13, 2021, doi: 10.1155/2021/7433186.

[14] Raad Z. Homod et al., "Deep clustering of Lagrangian trajectory for multi-task learning to energy saving in intelligent buildings using cooperative multi-agent," in Applied Energy , Volume 351, 1 December 2023, 121843, doi.org/10.1016/j.apenergy.2023.121843..

[15] Xingsi Xue et al., "A Novel partial sequence technique based Chaotic biogeography optimization for PAPR reduction in eneralized frequency division multiplexing waveform," in Heliyon, vol. 9, 2023, doi: 10.1016/j.heliyon.2023.e19451.

[16] B. S. Vandana, P. J. Antony & S. R. Alva, "Significant Feature Extraction Automated Framework for Cancer Diagnosis from Bone Histopathology Images", *International Conference on Advances in Computing, Communications and Informatics (ICACCI)*, Bangalore, India, Sep. 2018, pp. 1046-1051, doi: 10.1109/ICACCI.2018.8554534.

[17] D. T. Nguyen, J. K. Kang, T. D. Pham, G. Batchuluun & K. R. Park, "Ultrasound image-based diagnosis of malignant thyroid nodule using artificial intelligence", *Sensors*, vol. 20, no. 7, pp 1822, 2020 doi: 10.3390/ s20071822.

[18] C. Li et al., "A comprehensive review of computer-aided whole-slide image analysis: from datasets to feature extraction, segmentation, classification, and detection approaches," *arXiv preprint arXiv,* vol. 2102, 10553, 2021, doi: 10.48550/arXiv. 2102.10553.

[19] H. B. Arunachalam, R. Mishra, O. Daescu, K. Cederberg, D. Rakheja, A. Sengupta & P. Leavey, "Viable and necrotic tumor assessment from whole slide images of osteosarcoma using machine-learning and deep-learning models", *PloS One*, vol. 14, no. 4, pp. 1-19, 2019, doi: 10.1371/journal.pone.0210706.

[20] S. J. Badashah, S. S. Basha, S. R. Ahamed & S. P. V. Subba Rao, "Fractional-Harris hawks optimization-based generative adversarial network for osteosarcoma detection using Renyi entropy-hybrid fusion", *International Journal of Intelligent Systems*, vol. 36, no. 10, pp. 6007-6031, 2021, doi: 10.1002/int.22539.

[21] A. Lefteh, M. Houshmand, M. Khorrampanah & G. F. Smaisim, "Optimization of Modified Adaptive Neuro-Fuzzy Inference System (MANFIS) with Artificial Bee Colony (ABC) Algorithm for Classification of Bone Cancer" In *2022 Second International Conference on Distributed Computing and High Performance Computing (DCHPC)*, Qom, Islamic Republic of Iran, March 2022, pp. 78-81, doi: 10.1109/DCHPC55044.2022. 9731840

[22] S. B. Gurav, K. V. Kulhalli & V. V. Desai, "Fuzzy integrated salp swarm algorithm-based RideNN for prostate cancer detection using histopathology images" *Evolutionary Intelligence*, vol. 15, pp. 1329-1342, 2022, doi: 10.1007/s12065-020-00402-y.

[23] D. Shrivastava, S. Sanyal and AKMD. Kandar, "Bone cancer detection using machine learning techniques. In: Smart Healthcare for Disease Diagnosis and Prevention", *Smart Healthcare for Disease Diagnosis and Prevention*, pp 175-183, 2020, doi: 10.1016/B978-0-12-817913-0.00017-1.

[24] S. Santhanalakshmi, T. R. Abinaya, T. V. Affinasel and P. Dimple P, "Deep learning based bone tumor detection with real time datasets" *International Research Journal of Engineering and Technology (IRJET)*, vol. 7, no. 3, pp. 2391-2394, 2020.

[25] R. Agrawal, A. Kumar, S. A. AlQahtani, M. Maashi, O. Ibrahim Khalaf et al., "Cache memory design for single bit architecture with different sense amplifiers," Computers,

Materials & Continua, vol. 73, no.2, pp. 2313–2331,2022, doi: 10.32604/cmc.2022.029019.

[26] Y. Tao, X. Huang, Y. Tan, H. Wang, W. Jiang, Y. Chen, C. Wang, J. Luo, Z. Liu, K. Gao and W. Yang, “Qualitative histopathological classification of primary bone tumors using deep learning: a pilot study”, *Frontiers in oncology*, vol. 11, ID: 3969, Oct. 2021, doi: 10.3389/fonc.2021.735739.

[27] D. M. Anisuzzaman. H. Barzekar, L. Tong, J. Luo and Z. Yu, “A deep learning study on osteosarcoma detection from histological images”, *Biomedical Signal Processing and Control*, vol 69, ID; 102931, 2021, doi: 10.1016/j.bspc.2021.102931.

[28] Vandana BS, Alva SR, “Deep Learning Based Automated tool for cancer diagnosis from bone histopathology images”, *In 2021 International Conference on Intelligent Technologies (CONIT),* IEEE, Hubli, India, Jun 2021, pp. 1-8, doi: 10.1109/CONIT51480.2021.9498367.

[29] B. S. Vandana and S. R. Alva, "Deep Learning Based Automated tool for cancer diagnosis from bone histopathology images," *2021 International Conference on Intelligent Technologies (CONIT)*, Hubli, India, 2021, pp. 1-8, doi: 10.1109/CONIT51480.2021.9498367.

[30] S. K. Rana *et al*., "Decentralized Model to Protect Digital Evidence via Smart Contracts Using Layer 2 Polygon Blockchain," in *IEEE Access*, vol. 11, pp. 83289-83300, 2023, doi: 10.1109/ACCESS.2023.3302771.

[31] P. Bansal, K. Gehlot, A. Singhal and A. Gupta, “Automatic detection of osteosarcoma based on integrated features and feature selection using binary arithmetic optimization algorithm” *Multimedia Tools and Applications,* vol. 81, no. 6, pp. 8807-8834, Mar 2022, doi: 10.1007/s11042-022-11949-6.

[32] O. I. Khalaf, Ashokkumar, S. R., S. Dhanasekaran, G. M. Abdulsahib and Premkumar, M., “A decision science approach using hybrid EEG Feature Extraction and gan-based emotion classification,” *Advances in Decision Sciences*, vol 27, pp. 172-191, 2023, doi: 10.47654/v27y2023i1p172-191.Pages 172-191.